

Low voltage thin film transistors based on solution-processed In₂O₃:W. A remarkably stable semiconductor under negative and positive bias stress

Kosta Paxinos,¹ Giorgos Antoniou,¹ Dimitrios Afouxenidis,¹ Ahmed Mohamed¹, Umar Dikko¹, Ioannis Tsitsimpelis¹, William I. Milne², Arokia Nathan^{2,3} and George Adamopoulos^{1,a)}

¹ *Department of Engineering, Lancaster University, Lancaster LA1 4YR, UK*

² *Department of Engineering, University of Cambridge, 9 JJ Thomson Avenue, Cambridge CB3 0FA, UK*

³ *Cambridge Touch Technologies, 154 Cambridge Science Park Milton Road, Cambridge CB4 0GN, UK*

Keywords: Indium oxide, oxide semiconductors, bias stress, thin film transistors, spray pyrolysis

Abstract

We have investigated solution-processed tungsten-doped crystalline indium oxide (In₂O₃:W) as a function of the W content and their implementation in TFTs also employing spray coated Y₂O₃ gate dielectrics, and gold source and drain contacts. We showed that tungsten doping practically has no effect on the optical band gap whereas it shifts up the Urbach tail energy of In₂O₃:W films. The TFT performance employing In₂O₃:W channels also seems to decline at high tungsten concentration. Negative and positive bias stress under (dark) ambient conditions of TFTs employing In₂O₃:W(0.1 at%) showed remarkable improvement in their stability characteristics compared to the un-doped ones. This is evidenced by significantly smaller changes of the threshold voltage and subthreshold swing with insignificant change of the electron mobility that was practically unaffected under negative bias voltage. The negative bias stress results were interpreted in terms of the higher W-O bond dissociation energy compared

^{a)} Corresponding author. Email: g.adamopoulos@lancaster.ac.uk

to that of In-O, and the consequent oxygen vacancy suppression. However, the positive bias stability results in a reduced accumulation of electrons in the back channel due to atmospheric oxygen absorption. The results presented in this report demonstrate the potential for stable, low operational voltage, high performance metal oxide-based TFTs employing gate dielectrics also grown from solutions, at low manufacturing cost.

Thin film transistors (TFTs) based on metal oxide semiconductors have been attracting considerable attention over the last two decades as alternatives to a-Si due to their superior electrical performance coupled with optical transparency to visible light and mechanical flexibility. They have become highly desirable for applications in backplane electronics for active-matrix organic light-emitting diodes (AMOLEDs) including flexible displays and other newly emerging areas. Indeed, the performance of oxide-based TFTs, i.e. the carrier mobility, exceeds that of amorphous a-Si-based TFTs, and their stability characteristics exceeds that of organic semiconductors.

Amongst the family of metal oxide semiconductors, In_2O_3 has received particular attention as it combines high electron mobility ($160 \text{ cm}^2/\text{Vs}$),¹ wide band gap ($3.6 - 3.75 \text{ eV}$)² and high optical transmittance in the visible spectrum. In more In_2O_3 -based complex systems (such as InGaZnO or InZnO), the high electron mobilities originate from the indium oxide as In-O octahedra with an edge-sharing structure, remains in the amorphous state and the In^{3+} 5s orbitals form extended conduction-band minima.³

The major drawbacks however of polycrystalline In_2O_3 are related to the grain boundaries formation that cause electrical inhomogeneities and poor control of background carrier concentration that results in high off-currents. To suppress crystallization, several reports on TFTs implementing semiconducting channels based on In_2O_3 have focused on InGaZnO ,^{4,5,6,7,8}

InZrZnO,^{9,10} InHfZnO,^{11,12,13,14} InWZnO,¹⁵ InSiZnO,^{16,17} InScZnO,¹⁸ InTaZnO,¹⁹ InBZnO,²⁰ InCZnO,²¹ InGaO,²² InGeO,²³ InHfO,²⁴ InSiO,^{25,26} InWO,²⁷ and InZnO,^{28,29} however works on doped In₂O₃ have also been reported.^{25,30,31,32,33,34}

In most cases, those In₂O₃-based semiconductors have been processed by a large number of vacuum-based and potentially costly techniques such as Atomic Layer Deposition, Sputtering, Pulsed Laser deposition, and e-beam deposition. However there are a handful of reports where solution-based techniques such as inkjet³⁵ printing, and spray pyrolysis^{36,37} have also been employed.

In addition, considering that the TFTs' electrical stability strongly depends on the dielectric/semiconductor interface the choice of suitable dielectrics is equally of high importance as a high density of defects in the dielectric and dielectric/ channel interface will deteriorate the device performance and reliability.

Taking the above into consideration, here, we challenge the idea to explore the use of spray coating for the deposition of crystalline tungsten-doped In₂O₃ (In₂O₃:W) paired with an equally spray coated Y₂O₃ high-k dielectric. In contrast with the reported drawbacks associated with devices implementing polycrystalline thin films, this approach and deposition technique, produced devices with high performance and high TFT stability under both negative and positive bias stress. The choice of Y₂O₃ as the dielectric was mainly due to its moderately high-k dielectric value (in the range between 12 and 20),³⁸ good thermal stability, low leakage currents^{39,40} as well as due to its lattice constant $a=10.604 \text{ \AA}$,⁴¹ which is comparable to that of In₂O₃ (10.117 \AA).⁴²

In₂O₃:W films of typical thickness of about 12 nm were deposited by spray pyrolysis of indium chloride (InCl₃) solutions in methanol (0.01 M) at a substrate temperature of 400 °C. Tungsten doping was achieved by simple chemical blending of InCl₃ with the desired quantity of WCl₆

solution in methanol (0.02 M) and aerosols of the solutions were spray coated on Glass/ITO/Y₂O₃ stacks. Y₂O₃ gate dielectrics of typical thickness of 50 nm were similarly spray coated onto prepatterned ITO-coated glass substrates from yttrium(III) acetylacetonate hydrate [Y(CH₃COCHCOCH₃)₃·H₂O] solutions in methanol as described elsewhere.⁴³ In all cases, a conventional pneumatic airbrush (nozzle size 0.2 mm) operating at 4 bar was used. The airbrush was held at a vertical distance of about 20 cm above the substrate and after a 5 s spray coating period the spray process was interrupted for 20 s to allow for the vapors to settle. The cycle was repeated until films of the desired thicknesses were obtained. The dielectric properties of Y₂O₃ gate dielectrics of different thicknesses were investigated using a metal-insulator-metal (MIM) configuration with aluminum contacts of different areas (in the range between 0.025 mm² and 1 mm²) that were evaporated through a shadow mask onto glass/ITO/dielectric stacks. Similarly, aluminum metal source and drain electrodes were thermally evaporated under high vacuum through a series of shadow masks following In₂O₃:W deposition on the glass/ITO/Y₂O₃ gate stacks. The bottom-gate top contact TFTs were annealed at 120 °C in air and field effect and bias stress measurements were performed in dark under ambient conditions (T= 295 K, RH= 58 %). To further demonstrate the deposition technique's versatility and large-area compatibility, as well as the device fabrication reproducibility, 18 devices for each doping ratio have been fabricated under identical conditions and TFT architectures over a deposition area of 12 cm x 12 cm.

Initially, the optical properties of In₂O₃:W films on fused silica substrates were investigated by UV-Vis absorption spectroscopy at wavelengths between 200 nm and 1000 nm using an Agilent Cary 5000 spectrometer. The Tauc plots (data not shown) indicate that the direct transition is the dominant transition involved and the linear dependence in the semi-logarithmic representation equally reveals Urbach-type behavior that is attributed to a structural disorder causing an exponentially decaying density of localized states at the band edges. As illustrated

in Fig. 1, the optical band gap practically remains unaffected by the inclusion of tungsten, however the Urbach tail energy shows a monotonic increase as a function of the tungsten to indium ratio suggesting a stronger tail due to increased defect concentration with increasing tungsten content.

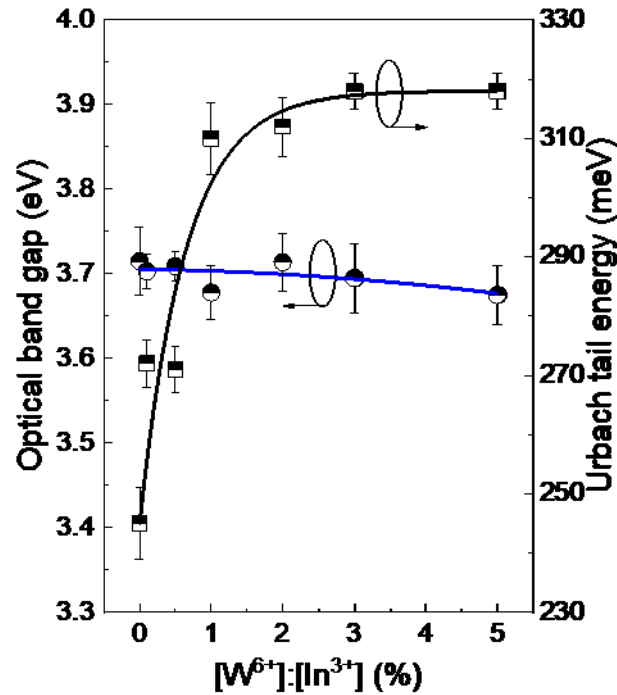


Fig. 1: Optical band gap and Urbach tail energy of $\text{In}_2\text{O}_3:\text{W}$ films as a function of the tungsten to In ratio (in the solution). The solid lines guide the eye.

The structure of the W-doped indium oxide films was further investigated by x-ray diffraction using a Rigaku SmartLab diffractometer with $\text{CuK}\alpha$ radiation operating at 45 kV and 200 mA equipped with a $\text{Ge}(220)\times 2$ monochromator, and a DteX250 1D detector. The XRD patterns (raw data) of W-doped In_2O_3 as well as the lattice constant and average crystal size as a function of the W doping level, are illustrated in Fig. 2.

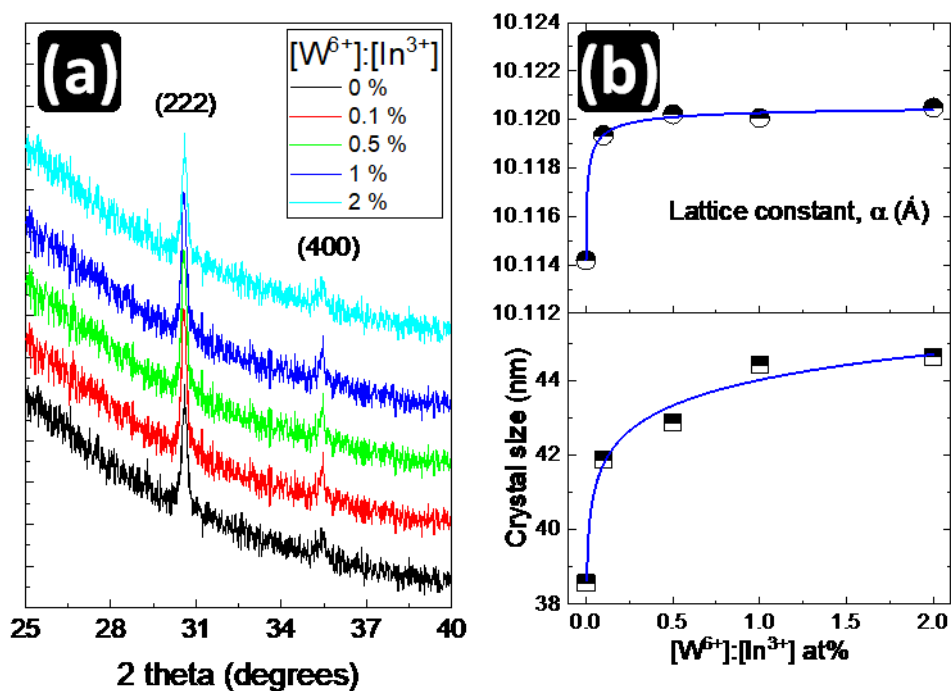


Fig. 2: a) XRD patterns and b) lattice constant and average crystal size of $\text{In}_2\text{O}_3:\text{W}$ as a function of the W doping level. The solid lines are guides to the eye.

The XRD patterns suggest polycrystalline cubic bixbyite structure (JCPDS no. 71-2195) In_2O_3 films exhibiting a preferred orientation along the (222) plane. The fact that no peaks associated to other compounds were detected, suggests that W doping hasn't altered the crystalline structure of In_2O_3 host. As equally depicted in Fig.2, W-doping results in a monotonic increase of the average crystal size whereas the lattice constant shows a sharp increase for small doping content (suggesting the In_2O_3 lattice expansion) reaching a plateau for higher doping levels. Assuming substitutional doping and given that the ionic radii of W^{4+} (66 pm), W^{5+} (62 pm) and W^{6+} (60 pm) are significantly lower than that of In^{3+} (81 pm) such lattice expansion should then be attributed to interstitial doping, in line with the increased average crystal size. Additionally, the observed lattice small however distinct expansion for increasing the W content could also be attributed to increased defects density and impurities as well as lattice mismatches as reported for $\text{In}_2\text{O}_3:\text{Mo}$.⁴⁴

Prior to the manufacture of the TFTs Y_2O_3 gate dielectrics were deposited on ITO-coated glass. The dielectric properties of the Y_2O_3 films are summarized in Fig. 3 where stable dielectrics of high capacitive density (218 nF/cm^2) and low leakage current density of about 10 nA/cm^2 (at 0.75 MV cm^{-1}) are illustrated.

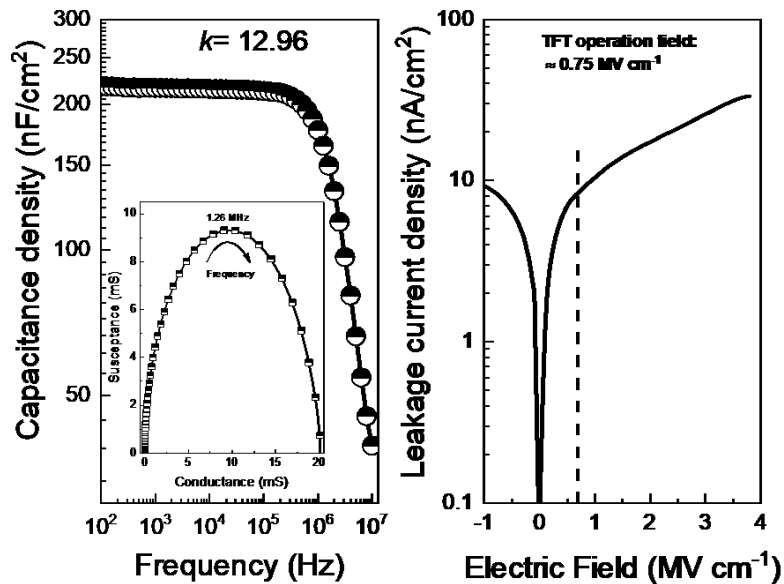


Fig. 3: a) Bode plot and b) leakage current density of solution processed Y_2O_3 gate dielectrics. Nyquist plot is show inset Fig. 3a.

Representative transfer characteristics, at saturation, of TFTs implementing $In_2O_3:W$ channels with different tungsten to indium ratio in the precursor solutions are depicted in Fig. 4a. Also the TFT parameters are summarized in Fig. 4b.

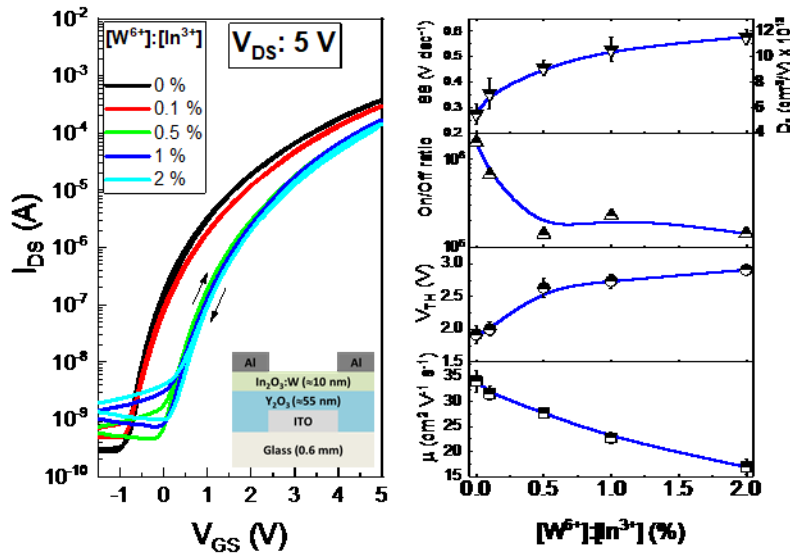


Fig. 4: a) Transfer characteristics (at saturation) of TFTs with $\text{In}_2\text{O}_3\text{:W}$ channels of different W content. b) TFT parameters as a function of the tungsten to indium content (in the solution).

The TFTs exhibit excellent operating characteristics with low voltage, negligible hysteresis, current on/off ratio in the range between 10^5 and 10^6 and electron mobilities in the range between $16 \text{ cm}^2 \text{ V}^{-1} \text{ s}^{-1}$ and $35 \text{ cm}^2 \text{ V}^{-1} \text{ s}^{-1}$ depending on the tungsten content. The TFT parameter variations are further supported by the Urbach tail energy monotonic increase as a function of the tungsten to indium content, as evidenced by the device performance change i.e. the monotonic increase of the threshold voltage and subthreshold swing (and the interfacial trap density) as well as the monotonic decrease of the TFT mobility and on-to-off current modulation ratio. Equally, the off-state current ratio increases monotonically at higher W-doping levels from 2.8×10^{-10} to 9.8×10^{-10} A (for the un-doped and heavily-doped films respectively) indicating the increased trap density for higher W-content, a finding that is supported by the subthreshold swing trend as well as the x-ray diffraction data. These TFT parameter trends denote oxygen vacancy suppression as previously reported for InGaZnO_4 and can be attributed to the higher W–O bonds dissociation energy (720 kJ mol^{-1}) with respect to that of In–O (346 kJ mol^{-1}). Hence W incorporation allows oxygen to compensate the oxygen-

deficient sites during the spray pyrolysis process. Similar results have been reported for TFTs with amorphous In-W-O deposited by DC magnetron sputtering.²⁷

Notably, and in spite the obvious performance decline of TFTs with high tungsten content, TFTs with In₂O₃:W(at. 0.1%) exhibit high performance in terms of electron mobility, compared to those using un-doped In₂O₃. Hence films of this doping level will be subject to further analysis.

To further examine the potential of In₂O₃:W-based TFTs, their stability under negative and positive bias was investigated. Fig. 5 shows the saturated transfer characteristics of TFTs with In₂O₃ and In₂O₃:W (at. 0.1%) channels subject to negative bias stress ($V_{GS} = -5$ V) in ambient conditions ($T = 295$ K, $RH = 58$ %) and dark for durations up to 10,000 s.

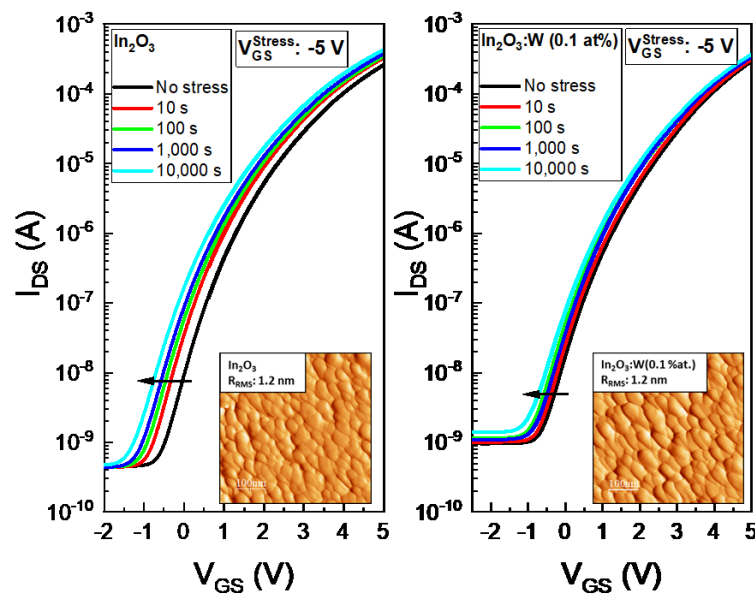


Fig. 5: A representative set of transfer characteristics after negative bias stress ($V_{GS} = -5$ V) of TFTs using a) un-doped In₂O₃ and b) In₂O₃:W(0.1 at%) semiconducting channels. Inset are the friction images of In₂O₃ and In₂O₃:W(0.1 at%) films.

Although, positive bias stress effects are less important since the resulting positive threshold voltage shift, if any, can be compensated by an external driver circuit, TFTs with In₂O₃ and In₂O₃:W(at. 0.1%) channels were subject to positive bias stress ($V_{GS} = 5$ V). Similarly, their

saturated transfer characteristics are illustrated in Fig. 6.

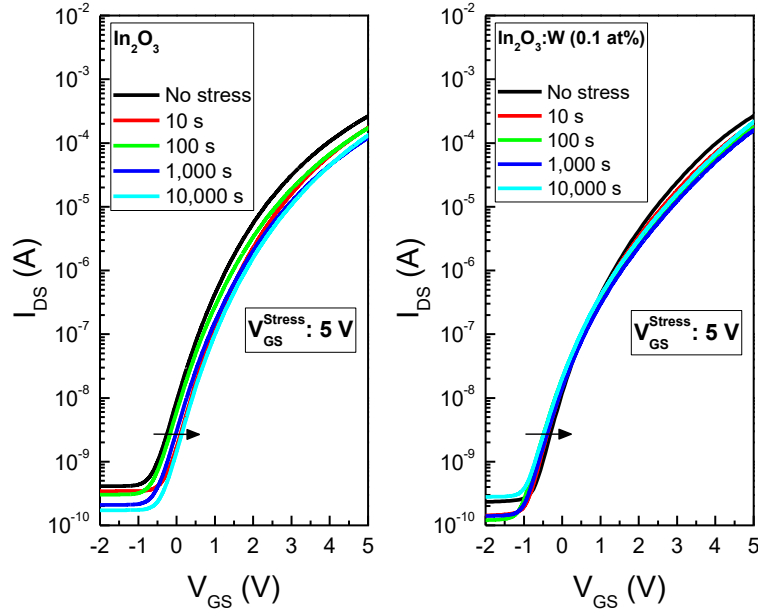


Fig. 6: A representative set of transfer characteristics after positive bias stress ($V_{GS}=5\text{ V}$) of TFTs with a) un-doped In_2O_3 and b) $\text{In}_2\text{O}_3:\text{W}(0.1\text{ at}\%)$ semiconducting channels.

The change of the main parameters after negative and positive bias stress of TFTs with un-doped In_2O_3 and $\text{In}_2\text{O}_3:\text{W}(0.1\text{ at}\%)$ semiconducting channels are summarized in Fig. 7. To note that the error bars represent the parameter's standard deviation of 18 distinct TFTs of the same channel length and width that were fabricated in different batches under identical conditions.

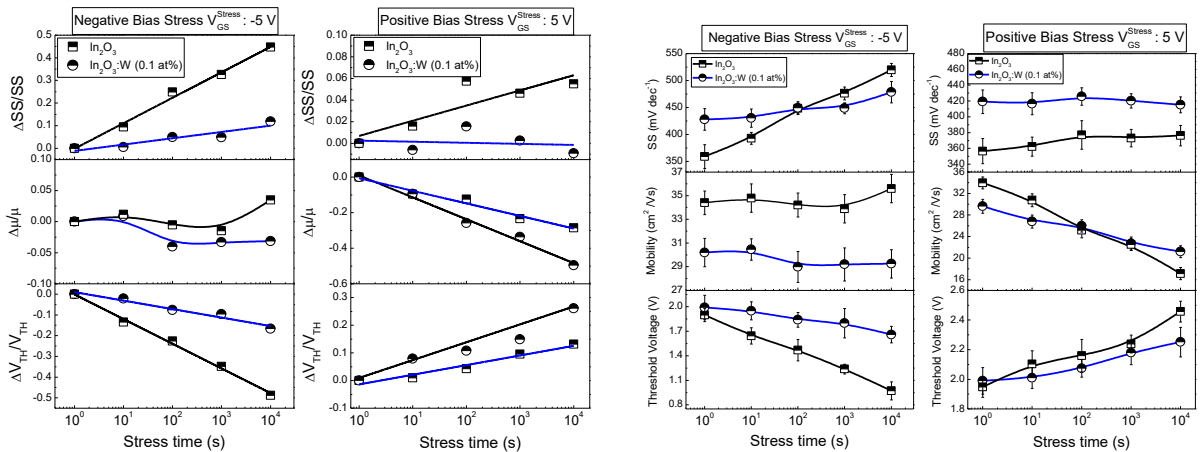


Fig.7: Left: Relative change of subthreshold swing, field effect mobility and threshold voltage of TFTs with un-doped In_2O_3 and $\text{In}_2\text{O}_3:\text{W}(0.1\text{ at}\%)$ channels as a function of the time under negative and positive bias stress. Right: Extracted TFT parameters as a function of the bias stress time (right).

In spite of the fact that no passivation layers were used, there was clearly negative bias stress stability improvement of devices with $\text{In}_2\text{O}_3:\text{W}(0.1 \text{ at}\%)$ channels compared to those with un-doped In_2O_3 (see Fig. 7). More precisely, the electron mobility remained virtually unchanged whereas the subthreshold swing as well as the threshold voltage showed significantly improved immunity to negative bias stress. As mentioned before, we attribute this to the higher W-O bond dissociation energy compared to that of In-O and the consequent oxygen vacancy suppression.

We would also like to point out that the stability under negative bias stress was further improved for devices with channels of higher W content (data not shown). However their electron mobility significantly dropped from $35 \text{ cm}^2 \text{ V}^{-1} \text{ s}^{-1}$ to $16 \text{ cm}^2 \text{ V}^{-1} \text{ s}^{-1}$ for un-doped In_2O_3 and $\text{In}_2\text{O}_3:\text{W}(2 \text{ at}\%)$, respectively. Although less prominent, W incorporation also improved the stability under positive bias stress, as depicted in Fig. 7. As expected, the threshold voltage shifts up toward positive voltages and has previously been attributed to oxygen-related electron-trapping states under positive bias. The considerable difference of the TFT parameters with and without channel doping is attributed to a number of factors such as electron trapping at the semiconductor/dielectric interface as well as atmospheric water vapor and O_2 absorption. The latter is considered as the most probable scenario due to the formation of a depletion layer on the back channel, resulting in a positive threshold voltage shift⁴⁷ and has been reported for very thin IGZO layers. Indeed, positive bias stress under ambient conditions, leads to excess electron accumulation in the channel layer as O_2 adsorption in the channel depletes electron carriers, which in turn shifts up the threshold voltage. In both cases, the considerable improvement of the subthreshold swing stability of the devices with W doped channels also reveals the limited defect creation at the channel/dielectric interface during bias stressing.

In conclusion, we have investigated solution-processed tungsten-doped crystalline indium oxide ($\text{In}_2\text{O}_3:\text{W}$) as a function of the W content and their implementation in TFTs also

employing spray coated Y_2O_3 gate dielectrics, and aluminum source and drain contacts. We showed that tungsten doping practically has no effect on the optical band gap whereas it shifts up the Urbach tail energy of $\text{In}_2\text{O}_3\text{:W}$ films. The TFT performance employing $\text{In}_2\text{O}_3\text{:W}$ channels also seems to decline at high tungsten concentration. Negative and positive bias stress under (dark) ambient conditions of TFTs employing $\text{In}_2\text{O}_3\text{:W}(0.1 \text{ at}\%)$ showed remarkable improvement in their stability characteristics compared to the un-doped ones. This is evidenced by significantly smaller changes of the threshold voltage and subthreshold swing with insignificant change of the electron mobility that was practically unaffected under negative bias voltage. The negative bias stress results were interpreted in terms of the higher W-O bond dissociation energy compared to that of In-O, and the consequent oxygen vacancy suppression. whereas the positive bias stability, in terms of a reduced accumulation of electrons in the back channel due to atmospheric oxygen absorption. The results presented in this report demonstrate the potential of the implementation of crystalline metal-oxide semiconductors based on $\text{In}_2\text{O}_3\text{:W}$, paired with Y_2O_3 gate dielectrics, for stable, low operational voltage, high performance TFTs deposited from solutions, at low manufacturing cost.

Acknowledgements

G. A. is grateful for support from the Royal Academy of Engineering and Leverhulme Trust (grant no. LTSRF1718\14\14).

References

¹ R.L. Weiher, J. Appl. Phys. **33**, 2834 (1962).

² R.L. Weiher and R.P. Ley, J. Appl. Phys. **37**, 299 (1966).

³ K. Nomura, T. Kamiya, H. Ohta, T. Uruga, M. Hirano, and H. Hosono, Phys. Rev. B **75**,

035212 (2007).

⁴ T. Kamiya, K. Nomura, and H. Hosono, *Sci. Technol. Adv. Mater.* **11**, (2010).

⁵ H. Yabuta, M. Sano, K. Abe, T. Aiba, T. Den, H. Kumomi, K. Nomura, T. Kamiya, and H. Hosono, *Appl. Phys. Lett.* **89**, 10 (2006).

⁶ K. Nomura, A. Takagi, T. Kamiya, H. Ohta, M. Hirano, and H. Hosono, *Jpn. J. Appl. Phys.* **45**, 4303 (2006).

⁷ M.S. Park, D.H. Lee, E.J. Bae, D.H. Kim, J.G. Kang, D.H. Son, and S.O. Ryu, *Mol. Cryst. Liq. Cryst.* **529**, 137 (2010).

⁸ J.-Y. Kwon, D.-J. Lee, and K.-B. Kim, *Electron. Mater. Lett.* **7**, 1 (2011).

⁹ J.S. Park, K. Kim, Y.G. Park, Y.G. Mo, H.D. Kim, and J.K. Jeong, *Adv. Mater.* **21**, 329 (2009).

¹⁰ P.T. Tue, T. Miyasako, J. Li, H.T.C. Tu, S. Inoue, E. Tokumitsu, and T. Shimoda, *IEEE Trans. Electron Devices* **60**, 320 (2013).

¹¹ E. Chong, K.C. Jo, and S.Y. Lee, *Appl. Phys. Lett.* **96**, 152102 (2010).

¹² T. Kim, S. Park, and S. Jeon, *Sci. Rep.* **7**, 1 (2017).

¹³ K. Ghaffarzadeh, A. Nathan, J. Robertson, S. Kim, S. Jeon, C. Kim, U.-I. Chung, and J.-H. Lee, *Appl. Phys. Lett.* **97**, 113504 (2010).

¹⁴ H.S. Choi, S. Jeon, H. Kim, J. Shin, C. Kim, and U.I. Chung, *Appl. Phys. Lett.* **99**, 2009 (2011).

¹⁵ T. Kizu, N. Mitoma, M. Miyanaga, H. Awata, T. Nabatame, and K. Tsukagoshi, *J. Appl. Phys.* **118**, 125702 (2015).

- ¹⁶ E. Chong, S.H. Kim, and S.Y. Lee, *Appl. Phys. Lett.* **97**, 252112 (2010).
- ¹⁷ J.Y. Choi, K. Heo, K.-S. Cho, S.W. Hwang, J. Chung, S. Kim, B.H. Lee, and S.Y. Lee, *Sci. Rep.* **7**, 15392 (2017).
- ¹⁸ J.W. Hennek, J. Smith, A. Yan, M.G. Kim, W. Zhao, V.P. Dravid, A. Facchetti, and T.J. Marks, *J. Am. Chem. Soc.* **135**, 10729 (2013).
- ¹⁹ N. Xiong, P. Xiao, M. Li, H. Xu, R. Yao, S. Wen, and J. Peng, *Appl. Phys. Lett.* **102**, 242102 (2013).
- ²⁰ S. Parthiban and J.-Y. Kwon, *J. Mater. Chem. C* **3**, 1661 (2015).
- ²¹ S. Parthiban and J.-Y. Kwon, *RSC Adv.* **4**, 21958 (2014).
- ²² G. Gonçalves, P. Barquinha, L. Pereira, N. Franco, E. Alves, R. Martins, and E. Fortunato, *Electrochem. Solid-State Lett.* **13**, H20 (2010).
- ²³ T. Maruyama and T. Tago, *Appl. Phys. Lett.* **64**, 1395 (1994).
- ²⁴ M.-F. Lin, X. Gao, N. Mitoma, T. Kizu, W. Ou-Yang, S. Aikawa, T. Nabatame, and K. Tsukagoshi, *AIP Adv.* **5**, 017116 (2015).
- ²⁵ S. Aikawa, T. Nabatame, and K. Tsukagoshi, *Appl. Phys. Lett.* **103**, 172105 (2013).
- ²⁶ N. Mitoma, S. Aikawa, X. Gao, T. Kizu, M. Shimizu, M.-F. Lin, T. Nabatame, and K. Tsukagoshi, *Appl. Phys. Lett.* **104**, 102103 (2014).
- ²⁷ T. Kizu, S. Aikawa, N. Mitoma, M. Shimizu, X. Gao, M.-F. Lin, T. Nabatame, and K. Tsukagoshi, *Appl. Phys. Lett.* **104**, 152103 (2014).
- ²⁸ P. Barquinha, A. Pimentel, A. Marques, L. Pereira, R. Martins, and E. Fortunato, *J. Non. Cryst. Solids* **352**, 1749 (2006).

- ²⁹ N.L. Dehuff, E.S. Kettenring, D. Hong, H.Q. Chiang, J.F. Wager, R.L. Hoffman, C.H. Park, and D.A. Keszler, *J. Appl. Phys.* **97**, 064505 (2005).
- ³⁰ R.R. Krishnan, V.S. Kavitha, S.R. Chalana, R. Prabhu, and V.P.M. Pillai, *JOM* **71**, 1885 (2019).
- ³¹ N. Mitoma, S. Aikawa, X. Gao, T. Kizu, M. Shimizu, M.F. Lin, T. Nabatame, and K. Tsukagoshi, *Appl. Phys. Lett.* **104**, (2014).
- ³² X. Li, Q. Zhang, W. Miao, L. Huang, Z. Zhang, and Z. Hua, *J. Vac. Sci. Technol. A Vacuum, Surfaces, Film.* **24**, 1866 (2006).
- ³³ S. Aikawa, T. Nabatame, and K. Tsukagoshi, *Jpn. J. Appl. Phys.* **58**, 090506 (2019).
- ³⁴ T. Kim, B. Jang, S. Lee, W.-Y. Lee, and J. Jang, *IEEE Electron Device Lett.* **39**, 1872 (2018).
- ³⁵ J.S. Lee, Y.-J. Kwack, and W.-S. Choi, *ACS Appl. Mater. Interfaces* **5**, 11578 (2013).
- ³⁶ L. Petti, H. Faber, N. Münzenrieder, G. Cantarella, P.A. Patsalas, G. Tröster, and T.D. Anthopoulos, *Appl. Phys. Lett.* **106**, 10 (2015).
- ³⁷ H. Faber, Y.H. Lin, S.R. Thomas, K. Zhao, N. Pliatsikas, M.A. McLachlan, A. Amassian, P.A. Patsalas, and T.D. Anthopoulos, *ACS Appl. Mater. Interfaces* **7**, 782 (2015).
- ³⁸ G. Adamopoulos, S. Thomas, D.D.C. Bradley, M.A. McLachlan, and T.D. Anthopoulos, *Appl. Phys. Lett.* **98**, 1 (2011).
- ³⁹ R.N. Sharma and A.C. Rastogi, *J. Appl. Phys.* **74**, 6691 (1993).
- ⁴⁰ M. Gurvitch, L. Manchanda, and J.M. Gibson, *Appl. Phys. Lett.* **51**, 919 (1987).
- ⁴¹ Y.N. Xu, Z. quan Gu, and W. Ching, *Phys. Rev. B - Condens. Matter Mater. Phys.* **56**, 14993 (1997).

- ⁴² M. Marezio, *Acta Crystallogr.* **20**, 723 (1966).
- ⁴³ G. Adamopoulos, S. Thomas, D.D.C. Bradley, M.A. McLachlan, and T.D. Anthopoulos, *Appl. Phys. Lett.* **98**, 123503 (2011).
- ⁴⁴ Y. Meng, X.L. Yang, H.X. Chen, J. Shen, Y.M. Jiang, Z.J. Zhang, and Z.Y. Hua, *Thin Solid Films* **394**, 218 (2001).
- ⁴⁵ K.H. Ji, J.I. Kim, H.Y. Jung, S.Y. Park, R. Choi, U.K. Kim, C.S. Hwang, D. Lee, H. Hwang, and J.K. Jeong, *Appl. Phys. Lett.* **98**, 103509 (2011).
- ⁴⁶ O. Seo, J. Chung, and J. Jo, *Eur. Phys. J. Appl. Phys.* **54**, 10302 (2011).
- ⁴⁷ W.-F. Chung, T.-C. Chang, H.-W. Li, S.-C. Chen, Y.-C. Chen, T.-Y. Tseng, and Y.-H. Tai, *Appl. Phys. Lett.* **98**, 152109 (2011).